PAPER • OPEN ACCESS

Uniaxial and fourfold basal anisotropy in GdRh$_2$Si$_2$

View the article online for updates and enhancements.

Uniaxial and fourfold basal anisotropy in GdRh$_2$Si$_2$

D Ehlers[1,2,4] , K Kliemt[3] , C Krellner[3], C Geibel[1] and J Sichelschmidt[1]

[1] Max-Planck-Institut für Chemische Physik fester Stoffe, 01187 Dresden, Germany
[2] Experimentalphysik V, Zentrum für elektronische Korrelationen und Magnetismus, Universität Augsburg, 86135 Augsburg, Germany
[3] Physikalisches Institut, Goethe-Universität Frankfurt am Main, 60438 Frankfurt am Main, Germany

E-mail: Dieter.Ehlers@physik.uni-augsburg.de

CrossMark

Abstract
The magnetocrystalline anisotropy of GdRh$_2$Si$_2$ is examined in detail via the electron spin resonance (ESR) of its well-localised Gd^{3+} moments. Below $T_N = 107$ K, long range magnetic order sets in with ferromagnetic layers in the (aa)-plane stacked antiferromagnetically along the c-axis of the tetragonal structure. Interestingly, the easy-plane anisotropy allows for the observation of antiferromagnetic resonance at X- and Q-band microwave frequencies. In addition to the easy-plane anisotropy we have also quantified the weaker fourfold anisotropy within the easy plane. The obtained resonance fields are modelled in terms of eigenoscillations of the two antiferromagnetically coupled sublattices. Conversely, this model provides plots of the eigenfrequencies as a function of field and the specific anisotropy constants. Such calculations have rarely been done. Therefore our analysis is prototypical for other systems with fourfold in-plane anisotropy. It is demonstrated that the experimental in-plane ESR data may be crucial for a precise knowledge of the out-of-plane anisotropy.

Keywords: antiferromagnetic resonance, magnetic anisotropy, rare earth compounds

(Some figures may appear in colour only in the online journal)

1. Introduction

Besides exchange interactions and the distribution of magnetic moments the magnetocrystalline anisotropy is one of the most crucial aspects for understanding the magnetic properties of a magnetic material and notably its ground state. From a practical point of view, rare earth elements are used to increase the anisotropy of ferromagnets. In fundamental research the physics of $4f$-electrons allows the study of a variety of phenomena, where strong spin–orbit interactions, helimagnetism, indirect exchange interactions and Kondo physics may be mentioned. In this work, the magnetocrystalline anisotropy of the tetragonal antiferromagnet GdRh$_2$Si$_2$ shall be in the

spotlight, because previous works showed that its magnetism can excellently be described by a mean-field model together with an Ising-chain model [1] and it has been established experimentally that its anisotropy is well accessible by means of electron spin resonance (ESR) [2].

GdRh$_2$Si$_2$ belongs to the family of compounds with ThCr$_2$Si$_2$-structure which has provided an immense field for studying heavy-fermion physics including quantum phase transitions and Kondo effect [3, 4]. CeCu$_2$Si$_2$, CePd$_2$Si$_2$ and URu$_2$Si$_2$ show quantum criticality associated with the transition between antiferromagnetic and nonmagnetic ground states upon applying pressure. The suppression of antiferromagnetism is considered to induce unconventional superconductivity [5]. In YbRh$_2$Si$_2$, on the other hand, the antiferromagnetism with Néel-temperature $T_N = 65$ mK [6] is suppressed by a small magnetic field and it has been suggested that its superconductivity below 2 mK is nonetheless the consequence of an antiferromagnetic instability at zero magnetic

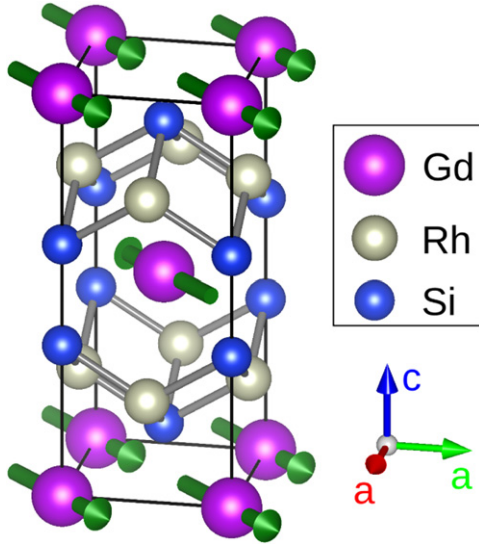[4] Author to whom any correspondence should be addressed.

Figure 1. The tetragonal crystal structure of $GdRh_2Si_2$ with the magnetic structure of Gd ions illustrated [11] by the green arrows lying in the (*aa*)-plane.

field [7]. While the *g*-factor is much larger in the tetragonal (*aa*)-plane than along the *c*-axis [8], suggesting an antiferromagnetic ground state order parameter within the plane, a precise experimental determination of this magnetic ground state is still lacking because of the weak magnetic moment and the low Néel-temperature [9, 10].

Considering this close structural and magnetic relation to $YbRh_2Si_2$, a thorough investigation of $GdRh_2Si_2$ by means of ESR seems even more interesting. The magnetic Gd^{3+}-ions form stacked square lattice layers in the crystallographic (*aa*)-plane with the individual ions being in a tetragonal coordination. The exchange coupling within the layers is of ferromagnetic sign, but the coupling between the layers, thus along the *c*-direction, is antiferromagnetic. The magnetic structure is depicted in figure 1. As the magnetic moments only consist of the spin part ($J = S = 7/2$), no large spin–orbit interaction may be expected and the value of the saturated moment, $\mu_s = 7\mu_B$, together with the lattice parameters yields a saturated sublattice magnetisation of $M_s = 400$ G. $GdRh_2Si_2$ has its Néel-temperature at $T_N = 107$ K, allowing an easy experimental access to the ordered state.

The magnetic anisotropy aligns the spins into the (*aa*)-plane as has been explained by a detailed analysis of magnetisation measurements [1]. The major contribution to anisotropy is thus uniaxial and of easy-plane type. Additionally, a second, weaker anisotropy selects ground-state magnetisation directions within this plane, which are the [110]-, [1$\bar{1}$0]-, [$\bar{1}\bar{1}$0]- and [$\bar{1}$10]-directions, see figure 1 for one possibility. On the other hand, this anisotropy term makes the spins to avoid the [100]-, [010]-, [$\bar{1}$00]- and [0$\bar{1}$0]-directions. This minor anisotropy contribution is consequently of fourfold symmetry around the *c*-axis. As it is responsible for the spin direction within the (*aa*)-plane, it is termed basal anisotropy. Due to the four possibilities for the magnetisation sublattices to align within the basal plane in zero and low magnetic fields, a domain structure is developed [1]. Thus, figure 1 shows only one of the magnetic domains and the other three domains are obtained by

rotating all the depicted spin vectors by 90°, 180° or 270° about the *c*-axis. The ESR in $GdRh_2Si_2$ could be followed far inside the ordered regime [2], both at X-band and Q-band frequency. High-field ESR therefore seems unnecessary in this system and it is the aim of this work to quantify both terms of magnetocrystalline anisotropy at several temperatures $T < T_N$ using a conventional ESR setup. In our ESR experiments, especially in all the Q-band experiments, the magnetic fields of interest are large enough to have only one single antiferromagnetic domain. Hence, the domain suppression effects do not disturb the evaluated resonances.

The theoretical description of the anisotropy shall be by the classical theory of antiferromagnetic resonance where the eigenfrequencies of two coupled, oscillating magnetisation sublattices are evaluated. More precisely, we are mainly interested in resonance fields of our ESR data for a given oscillation frequency. Nevertheless, calculated resonance frequencies as a function of external field are presented at the end of this report, giving additional insight into antiferromagnetic resonance in the presence of both uniaxial and fourfold basal anisotropy.

2. Methods

2.1. Sample preparation

The growth of the single crystals of $GdRh_2Si_2$ and their characterisation are explained in reference [12]. We used a platelet shaped sample with an area of about 1×1.3 mm^2 and a thickness of about 0.5 mm.

2.2. ESR spectroscopy

Continuous-wave ESR was performed both at a frequency of $\nu_{rf} = 34$ GHz (Q-band) and at 9.4 GHz (X-band). A Bruker Elexsys II spectrometer was used. In case of the Q-band experiments the resonator was a cylindrical Bruker ER5106QTW cavity and for X-band measurements the resonator used was a rectangular Bruker ER4122SHQ. In both cases a helium gas-flow cryostat allowed a temperature stability of less than 1 K. To measure the angular dependence in the naturally grown (*aa*)-plane, the samples were mounted with their growth plane perpendicular to the rotation axis of a goniometer. In order to perform rotations in the (*ac*)-plane, an *a*-axis was aligned parallel with the rotation axis, the sample being glued on a vertical facet of a glass holder. The external field $\boldsymbol{H}_0$ was swept up to 1.8 T. The spectra shown in this work are the first derivative of the absorbed microwave power, owing to the use of lock-in technique with field modulation.

2.3. Anisotropy simulations

Looking for the eigenoscillations of two antiferromagnetically coupled magnetisation sublattices, these two magnetisations are written as $\boldsymbol{M}^{(i)} = \boldsymbol{M}_0^{(i)} + \boldsymbol{m}^{(i)}$ with $i = 1, 2$, meaning a decomposition into their static parts (index 0) and dynamic parts (small letters), where $\left|\boldsymbol{m}^{(i)}\right| \ll \left|\boldsymbol{M}_0^{(i)}\right|$. Their equations of motion read

$$\mathrm{i}\omega\boldsymbol{m}^{(1)} + \gamma\boldsymbol{m}^{(1)} \times \boldsymbol{H}_{\mathrm{eff}0}^{(1)} + \gamma\boldsymbol{M}_0^{(1)} \times \boldsymbol{h}_{\mathrm{eff}}^{(1)} = 0, \qquad (1)$$

$$i\omega \boldsymbol{m}^{(2)} + \gamma \boldsymbol{m}^{(2)} \times \boldsymbol{H}_{\text{eff}0}^{(2)} + \gamma \boldsymbol{M}_0^{(2)} \times \boldsymbol{h}_{\text{eff}}^{(2)} = 0. \tag{2}$$

Here, $\boldsymbol{H}_{\text{eff}\,0}^{(i)}$ and $\boldsymbol{h}_{\text{eff}}^{(i)}$ are the static and dynamic effective fields acting on the respective sublattice i with $\left|\boldsymbol{h}_{\text{eff}}^{(i)}\right| \ll \left|\boldsymbol{H}_{\text{eff}\,0}^{(i)}\right|$, and γ is the gyromagnetic ratio. Equations (1) and (2) are derived from the respective Landau–Lifshitz equations by linearising in the small quantities $\boldsymbol{m}^{(i)}$ and $\boldsymbol{h}_{\text{eff}}^{(i)}$ and by setting the damping to zero [13]. Effective fields are expressed via the free energy density F:

$$H_{\text{eff}\,\alpha}^{(i)} = -\frac{\partial F}{\partial M_\alpha^{(i)}}, \quad H_{\text{eff}0}^{(i)} = H_{\text{eff}}^{(i)}\Big|_{\boldsymbol{m}=0}, \quad h_{\text{eff}\,\alpha}^{(i)} = \sum_\beta \frac{\partial H_{\text{eff}\,\alpha}^{(i)}}{\partial m_\beta^{(i)}}\Big|_{\boldsymbol{m}=0} m_\beta^{(i)}, \tag{3}$$

where α and β denote Cartesian components x, y, z. The internal energy in the system to be investigated by ESR consists of exchange energy F_{e}, Zeeman energy F_{Z}, uniaxial anisotropy energy F_{u} and basal anisotropy energy F_{b}:

$$\begin{aligned}
U &= F_{\text{e}} + F_{\text{Z}} + F_{\text{u}} + F_{\text{b}} \\
&= \Lambda \boldsymbol{M}_1 \cdot \boldsymbol{M}_2 - \boldsymbol{H}_0 \cdot (\boldsymbol{M}_1 + \boldsymbol{M}_2) \\
&\quad + K_{\text{u}}(\sin^2 \theta_1 + \sin^2 \theta_2) + K_{\text{b}}[\sin^2(2\varphi_1) + \sin^2(2\varphi_2)].
\end{aligned} \tag{4}$$

Here, Λ is the dimensionless antiferromagnetic exchange constant, $\boldsymbol{H}_0$ the external magnetic field, K_{u} the first order uniaxial anisotropy constant and K_{b} the first order basal anisotropy constant. The definitions of the polar angles θ_i correspond, in figure 2(a), to the angles between the $\boldsymbol{M}^{(i)}$ and the axis of uniaxial anisotropy (z-axis), and the azimuthal angles φ_i are, as is illustrated in that same sketch, defined within the (aa)-plane. Note that the above definition of basal anisotropy energy matches the one in reference [1].

With $M_0 = \left|\boldsymbol{M}_0^{(1)}\right| = \left|\boldsymbol{M}_0^{(2)}\right|$ and z_0 as the unit vector along z, the effective fields are, again after linearising in the $\boldsymbol{m}^{(i)}$,

$$\begin{aligned}
\boldsymbol{H}_{\text{eff}0}^{(1)} &= -\Lambda \boldsymbol{M}_0^{(2)} + \boldsymbol{H}_0 + \frac{2K_{\text{u}}}{M_0^2} z_0 \left(\boldsymbol{M}_0^{(1)} \cdot z_0\right) + \boldsymbol{H}_{\text{b}\,0}^{(1)}, \\
\boldsymbol{h}_{\text{eff}}^{(1)} &= -\Lambda \boldsymbol{m}^{(2)} + \frac{2K_{\text{u}}}{M_0^2} z_0 \left(\boldsymbol{m}^{(1)} \cdot z_0\right) + \boldsymbol{h}_{\text{b}}^{(1)}, \\
\boldsymbol{H}_{\text{eff}0}^{(2)} &= -\Lambda \boldsymbol{M}_0^{(1)} + \boldsymbol{H}_0 + \frac{2K_{\text{u}}}{M_0^2} z_0 \left(\boldsymbol{M}_0^{(2)} \cdot z_0\right) + \boldsymbol{H}_{\text{b}\,0}^{(2)}, \\
\boldsymbol{h}_{\text{eff}}^{(2)} &= -\Lambda \boldsymbol{m}^{(1)} + \frac{2K_{\text{u}}}{M_0^2} z_0 \left(\boldsymbol{m}^{(2)} \cdot z_0\right) + \boldsymbol{h}_{\text{b}}^{(2)}.
\end{aligned} \tag{5}$$

The effective fields of basal anisotropy, $\boldsymbol{H}_{\text{b}\,0}^{(i)}$ and $\boldsymbol{h}_{\text{b}}^{(i)}$, will be explained below for the two cases of field rotation separately. Equations (1) and (2) define in this way a coupled linear equation system, with six independent variables, namely the three Cartesian components of the two dynamic magnetisations $\boldsymbol{m}^{(i)}$. Defining a 6×6-matrix A, this is summarised as

$$A \begin{pmatrix} \boldsymbol{m}_1 \\ \boldsymbol{m}_2 \end{pmatrix} = 0. \tag{6}$$

In order to get nontrivial solutions, we set $\det A = 0$, providing either resonance frequencies ν_{res} for a given field or resonance
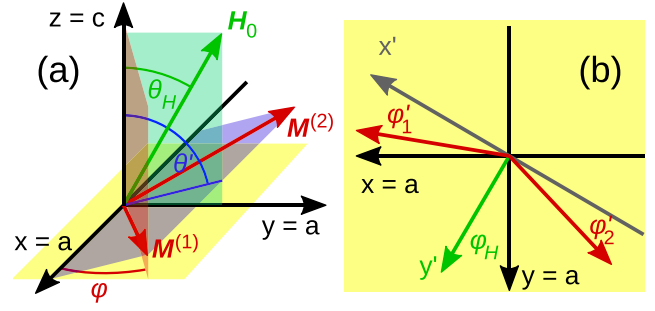

Figure 2. (a) Illustration of the field and magnetisation geometry when the external field $\boldsymbol{H}_0$ is within the (ac)-plane [here: (yz)-plane]. The external field spans an angle of θ_{H} with the z-axis. Sublattice magnetisations $\boldsymbol{M}^{(1)}$ and $\boldsymbol{M}^{(2)}$ lie symmetrically with respect to the (yz)-plane. Their common plane (violet) defines the angle θ' to the z-axis, which is not the same as the angle $\theta := \theta_1 = \theta_2$ spanned between the $\boldsymbol{M}^{(i)}$ and z. The basal anisotropy energy is defined via the azimuthal angle φ *within* the (aa)-plane, and in the case shown $\varphi := \varphi_1 = \varphi_2$. (b) For the field within (aa)-plane, it is convenient to define $y' \parallel \boldsymbol{H}_0$. φ_1' and φ_2' are then measured against the x'-axis. φ_{H} is measured between $\boldsymbol{H}_0$ and the y-axis.

fields H_{res} for a given microwave frequency. Of particular interest are two special cases, for which (6) is solved analytically [13] for $K_{\text{u}} < 0$ as is the case in GdRh$_2$Si$_2$: firstly, when $K_{\text{b}} = 0$ and $\boldsymbol{H}_0$ is in the basal plane, one of the two resonance frequencies is

$$\omega_{\text{res}} = \gamma H_0 \sqrt{1 - K_{\text{u}}/(\Lambda M_0^2)}, \tag{7}$$

where $H_0 = |\boldsymbol{H}_0|$. This value is very close to the paramagnetic value $\omega_{\text{res}} = \gamma H_0$ as long as the exchange field ΛM_0 is large as compared to the anisotropy field $H_{\text{u}} = 2K_{\text{u}}/M_0$. Secondly, for $K_{\text{b}} = 0$ and with $\boldsymbol{H}_0$ along the c-axis, one of the resonances occurs at $\omega_{\text{res}} = 0$, corresponding to a Goldstone mode, which is provided from the spontaneous symmetry breaking by the antiferromagnetic order parameter.

2.3.1. Out-of-plane rotations. When rotating the field within the (ac)-plane, and as long as we deal with the static field and magnetisation parts only, we may benefit from the mirror symmetry with respect to the (ac)-plane (see figure 2(a)) and write $\theta = \theta_1 = \theta_2$ as well as $\varphi = \varphi_1 = \varphi_2$. For further calculations, it is convenient to introduce a primed coordinate system x', y', z' with $x' = x$, but tilted by the angle $90° - \theta'$ towards $\boldsymbol{H}_0$, having y' within the purple plane of figure 2(a) and z' perpendicular to it. Now we introduce the angles $\varphi' = \sphericalangle(\boldsymbol{M}^{(1)}, x') = \sphericalangle(\boldsymbol{M}^{(2)}, -x')$, $\theta' = \sphericalangle(y', z)$ and $\delta = \sphericalangle(\boldsymbol{M}^{(1)}, \boldsymbol{H}_0) = \sphericalangle(\boldsymbol{M}^{(2)}, \boldsymbol{H}_0)$. The relationships between convenient angles θ', φ' and the angles θ, φ and δ used in (4) read

$$\begin{aligned}
\cos \theta &= \cos \theta' \sin \varphi', \\
\sin \varphi &= \tan \theta' \cot \theta, \\
\cos \varphi' &= \sin \theta \cos \varphi, \\
\cos \delta &= \sin \varphi' \cos (\theta' - \theta_{\text{H}}).
\end{aligned} \tag{8}$$

In this way, the free energy is expressed in terms of θ' and φ' as

$$F = -\Lambda M_0^2 \; \cos \; 2\varphi' - 2H_0M_0 \; \sin \; \varphi' \; \cos(\theta' - \theta_{\mathrm{H}})$$

$$- 2K_{\mathrm{u}} \; \cos^2 \; \theta' \; \sin^2 \; \varphi' + 2K_{\mathrm{b}} \frac{\sin^2 \; 2\varphi' \; \sin^2 \; \theta'}{\left(1 - \cos^2 \; \theta' \; \sin^2 \; \varphi'\right)^2}.$$

(9)

The two equilibrium angles θ'_0 and φ'_0 are found via the minimum of F.

When setting up the matrix A as defined by (6), however, the two sublattices with the respective effective fields acting on them need to be treated separately and the contracted form (9) for F is not suitable. Moreover, F shall be represented in a Cartesian form. In the primed coordinate system, $H_0 = \left(0, \cos\left(\theta'_0 - \theta_{\mathrm{H}}\right), \sin\left(\theta'_0 - \theta_{\mathrm{H}}\right)\right)$, $M_0^{(1)} = (\cos \; \varphi'_0, \sin \; \varphi'_0, 0)$, $M_0^{(2)} = (-\cos \; \varphi'_0, \sin \; \varphi'_0, 0)$, $z_0 = (0, \cos \theta'_0, \sin \theta'_0)$ and the calculation of the matrix A using the equations of motion (1), (2) and the effective fields (5) is straightforward, except for the basal anisotropy fields.

With $M^{(i)} = \left(M_x^{(i)}, M_y^{(i)}, M_z^{(i)}\right)$ in the unprimed system and $M^{(i)} = \left(M_{x'}^{(i)}, M_{y'}^{(i)}, M_{z'}^{(i)}\right)$ in the primed system we have $M_x^{(i)} = M_{x'}^{(i)}$, $M_y^{(i)} = M_{y'}^{(i)} \; \sin \; \theta'_0 - M_{z'}^{(i)} \; \cos \; \theta'_0$. From figure 2(a) follows

$$\sin \; \varphi_i = \frac{M_y^{(i)}}{\left[\left(M_x^{(i)}\right)^2 + \left(M_y^{(i)}\right)^2\right]^{1/2}}.$$

(10)

Note that now φ_i stands for the azimuthal angle due to both static and dynamic magnetisation parts. The two parts i of the basal anisotropy energy U_{b} in (4) are then expressed in a Cartesian way as

$$U_{\mathrm{b}i} = K_{\mathrm{b}} \; \sin^2 \; 2\varphi_i = 4K_{\mathrm{b}} \frac{\left(M_{x'}^{(i)}\right)^2 \left(M_{y'}^{(i)} \; \sin \; \theta'_0 - M_{z'}^{(i)} \; \cos \; \theta'_0\right)^2}{\left[\left(M_{x'}^{(i)}\right)^2 + \left(M_{y'}^{(i)} \; \sin \; \theta'_0 - M_{z'}^{(i)} \; \cos \; \theta'_0\right)^2\right]^2},$$

(11)

where static and dynamic magnetisation parts are still unseparated. Effective field components $H_{\mathrm{b}\,\alpha'}^{(i)}$ in direction α' are obtained as $H_{\mathrm{b}\,\alpha'}^{(i)} = -\partial F/\partial M_{\alpha'}^{(i)}$. Magnetisation components are subsequently separated into static and dynamic parts. Following (3), the static parts of the field components $H_{\mathrm{b}\,0\,\alpha'}^{(i)}$ are given by setting $m = 0$ and the dynamic field components $h_{\mathrm{b}\,\alpha'}^{(i)}$ are obtained as linearisations in the $m_{\alpha'}^{(i)}$. The assumption $M_{y'\,0}^{(i)} \ll M_{x'\,0}^{(i)}$, reflecting that the exchange field is the dominating interaction gives important simplifications. Concerning the static parts of the two sublattices, the only difference between them is the reversed static x-component: $M_{0\,x'}^{(2)} = -M_{0\,x'}^{(1)}$.

The resulting terms needed for the calculation of θ'_0, φ'_0 and A are documented in appendix A.

2.3.2. In-plane rotations. Following figure 2(b), the primed coordinate system is now defined by $z' = z$, but with $y' \parallel H_0$, being thus rotated by the angle φ_{H} around z with respect to the unprimed framework. The static part of the total magnetic energy may be written

$$F = -\Lambda M_0^2 \; \cos(\varphi'_1 + \varphi'_2) - H_0M_0 \; \sin \; \varphi'_1 - H_0M_0 \; \sin \; \varphi'_2$$

$$+ K_{\mathrm{u}} \left(\sin^2 \; 90^\circ + \sin^2 \; 90^\circ\right)$$

$$+ K_{\mathrm{b}} \left\{\sin^2 \left[2(\varphi'_1 - \varphi_{\mathrm{H}})\right] + \sin^2 \left[2(\varphi'_2 + \varphi_{\mathrm{H}})\right]\right\}.$$

(12)

Now the equilibrium angles $(\varphi'_1)_0$ and $(\varphi'_2)_0$ are found as the ones minimising F.

In the primed coordinate system $H_0 = (0, H_0, 0)$, $M_0^{(1)} = (M_0 \; \cos(\varphi'_1)_0, M_0 \; \sin(\varphi'_1)_0, 0)$ and $M_0^{(2)} = (-M_0 \; \cos(\varphi'_2)_0, M_0 \; \sin(\varphi'_2)_0, 0)$. As before, exchange, Zeeman and uniaxial terms in (1), (2) and (5) can be easily calculated. The basal anisotropy energy shall again be expressed in terms of Cartesian magnetisation components, so that basal terms can be introduced into matrix A, too. The angles φ'_1 and φ'_2 are regarded as due to both static and dynamic magnetisation. The K_{b}-term in (12) is expanded into sines and cosines of only φ'_1 or φ'_2, and using the just mentioned representations of the $M_0^{(i)}$, the basal energy parts become

$$F_{\mathrm{b}\,i} = K_{\mathrm{b}}/M_0^4 \left\{2M_{x'}^{(i)}M_{y'}^{(i)} \; \cos \; 2\varphi_{\mathrm{H}} \right.$$

$$\left. - \left[\left(M_{x'}^{(i)}\right)^2 - \left(M_{y'}^{(i)}\right)^2\right] \sin \; 2\varphi_{\mathrm{H}} \right\}^2.$$

(13)

Here again, $H_{\mathrm{b}\alpha'} = -\partial U/\partial M_{\alpha'}$. The procedure is then completely analogous to the out-of-plane treatment: separation into static and dynamic magnetisations, determination of effective fields as described by (3) using approximations $M_{y'\,0}^{(i)} \ll M_{x'\,0}^{(i)}$ and construction of A's matrix entries following (1), (2), (5) and (6). Note that, unlike the out-of-plane case, in general $M_{x'}^{(2)} \neq -M_{x'}^{(1)}$ and $M_{y'}^{(2)} \neq M_{y'}^{(1)}$.

Appendix B lists the detailed terms used in the calculation of $(\varphi'_1)_0$, $(\varphi'_2)_0$ and A.

2.3.3. Numerical procedure. When plotting resonance frequencies against magnetic field, it is sufficient to once calculate the equilibrium directions of sublattice magnetisations for given parameters and subsequently compute the resonance frequency. It turned out to be helpful to start with the highest field and then reduce the field in the plot, because at lowest fields other solutions than the physically observed ones may be captured as will be discussed below. When plotting resonance fields versus a field angle (either θ_{H} or φ_{H}) for a given microwave frequency, equilibrium directions and resonance fields need to be computed iteratively, because magnetisation directions depend on the resonance field and vice versa.

In either case the starting point for the resonance condition is the analytical expression (7), which is valid for $H_0 \parallel a$ and $K_{\mathrm{b}} = 0$. Therefore, calculations start with these parameters and the first field angle (other than $\theta_{\mathrm{H}} = 90^\circ$, $\varphi_{\mathrm{H}} = 0^\circ$) as well as K_{b} are switched on in small steps. Azimuthal angles φ' are initialized with the value $H_0/(\Lambda M_0)$.

Zeros of $\det A$, providing the resonance condition, as well as the zeros of (9) and (12), providing equilibrium angles, are implemented by the (one-/two-dimensional) Newton method. The derivatives of $\det A$ are computed by difference approximations either in ω or H_0. The derivatives needed for equilibrium angles are given analytically in the appendix.
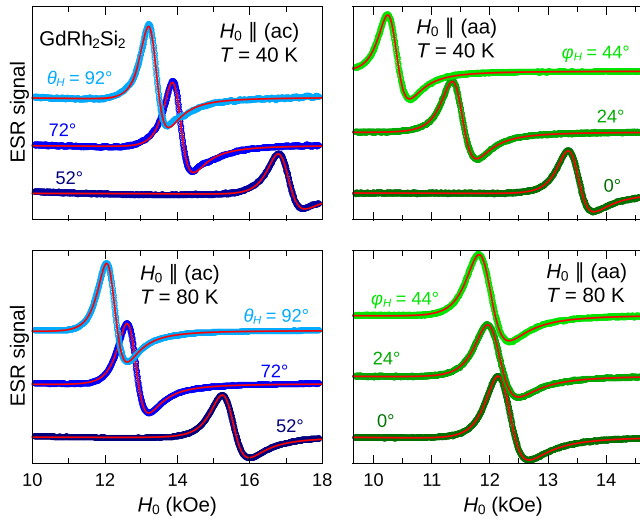
Figure 3. Q-band ESR-spectra of the GdRh$_2$Si$_2$ single crystal. The static magnetic field was rotated in the (*ac*)-plane (left frames) and in the (*aa*)-plane (right frames). The temperature of 40 K (upper frames) is compared to the temperature of 80 K (lower frames). Solid lines: fit curves by a single asymmetric Lorentzian derivative.

Figure 4. Q-band resonance fields from rotations within the (*ac*)-plane at temperatures between 20 and 80 K. $\theta_H = 0°$ means $H_0 \parallel c$ and $\theta_H = 90°$ corresponds to $H_0 \parallel a$. Solid lines: fits to the measured data, see main text and the fit parameters in figure 6(a).

3. Results and discussion

3.1. ESR anisotropy in the ordered regime

A few representative ESR spectra from the antiferromagnetically ordered state in GdRh$_2$Si$_2$ are plotted in figure 3, showing the field derivative of the absorbed microwave power, dP_{abs}/dH_0, versus the external field H_0. The fits use an asymmetric Lorentzian derivative, where the asymmetry is due to the conductivity of the sample [2]. The asymmetric lineshape indeed physically makes sense, because the penetration depth amounts to about 3 μm in the paramagnetic regime [14], much smaller than the thickness of the sample of about 0.5 mm. A dropping resistivity below T_N towards about 3 $\mu\Omega$cm at $T = 5$ K [12] results in even smaller penetration depths in the ordered state. It is seen that these fits provide an excellent description of the measured spectra, confirming the idea of well-localised and strong Gd^{3+} magnetic moments. Obtained parameters are the resonance field H_{res}, the linewidth ΔH, the asymmetry ratio D/A and the line intensity I, which corresponds to the area under the non-derived spectrum. While the focus shall here be on the resonance fields, it is noteworthy that the linewidth, in the range of 400 Oe, typically increases with increasing resonance field, as is also observed in the ordered states of many other localised-moment magnets [15–17]. D/A mostly assumes values between 0.5 and 1.0, in accordance with the expectation for a conductive system. Concerning H_{res}, a clear anisotropy is distinguished when rotating the external field out of plane (left frames in figure 3), but also within the (*aa*)-plane (right frames). The figure demonstrates that decreasing temperature enhances the magnetocrystalline anisotropy, which is because the sublattice magnetisations approach their saturated values.

The resonance fields for out-of-plane rotations at different temperatures are shown in figure 4. At the temperature of 80
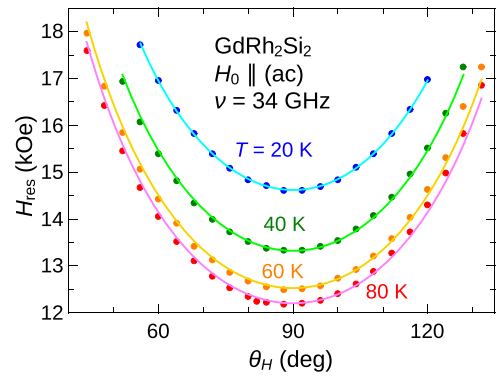
K and at $\theta_H = 90°$, meaning that the field is along the *a*-axis, the resonance field amounts to 12.2 kOe, close to the value of 12.1 kOe given for a paramagnetic moment with $g = 2$ at the frequency $\nu_{\mathrm{rf}} = 34$ GHz. Following (7), which holds for this field direction as long as basal anisotropy is negligible and when uniaxial anisotropy is much smaller than the exchange field, the paramagnetic value is indeed expected here. Resonance fields diverge when approaching $H_0 \parallel c$ and the observation of the resonance gets limited by the largest possible external field. As the resonance fields increase with decreasing temperature, only an angular range of $\pm30°$ around the *a*-axis is covered at $T = 20$ K. Diverging resonance fields for $H_0 \parallel c$ indicate that for a fixed external field the resonance frequency gets suppressed down to zero, thus reaching the Goldstone mode which cannot be observed experimentally. We can conclude that the quasi-paramagnetic mode at $\theta_H = 90°$ in easy-plane antiferromagnets with resonance condition (7) transforms continuously into the Goldstone mode also mentioned in section 2.3 when tilting towards the hard axis. Resonance fields at $T = 5$ K were analyzed, too, but are not displayed here because of a vanishing ESR signal over a wide angular range.

Fit curves in figure 4 demonstrate that the theoretical model of coupled oscillating magnetisation sublattices satisfactorily describes the measured data. Free fit parameters are only K_u and K_b and the g-factor is fixed to $g = 2$. Other parameters, which are supplied by external measurements, are the microwave frequency ν_{rf}, the sublattice magnetisations M_0 and the exchange constant Λ. We calculate the temperature dependence of M_0 as $M_0(T) = M_s\sqrt{1 - T/T_N}$ with the saturation value $M_s = 400$ G which one gets for the Gd^{3+} moment $\mu = 7\,\mu_B$ using lattice constants given in reference [12]. Λ can be calculated within a mean-field theory from the Néel-temperature T_N, the Curie–Weiss-temperature Θ_{CW} and the Curie constant C as $\Lambda = (T_N + \Theta_{\mathrm{CW}})/C = 710$ [18]. The fitted anisotropy constants are discussed in section 3.2.

In-plane resonance fields are shown in figure 5. Here, a four-fold anisotropy is clearly visible. From the point of view of the uniaxial anisotropy, the (*aa*)-plane is an easy plane, but the
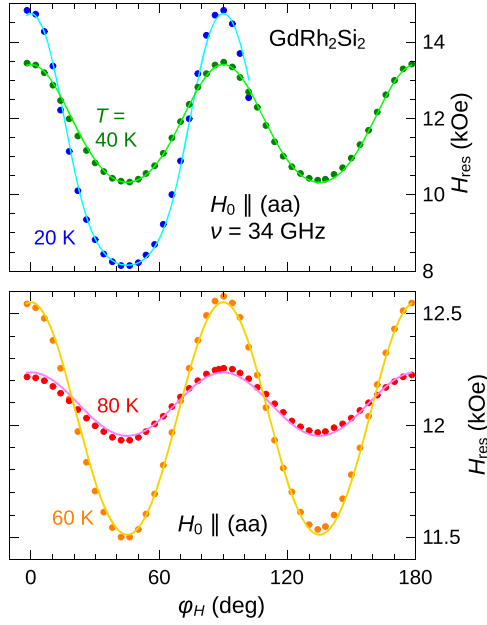
Figure 5. Q-band resonance fields from rotations within the (*aa*)-plane at temperatures between 20 and 80 K. $\varphi_H = 0°$ means $H_0 \parallel a$. Solid lines: fits to the measured data, see main text and the fit parameters in figure 6(b). High temperature and low temperature data are shown separately due to the different ordinate scales.

Figure 6. (a) The negative of the uniaxial anisotropy constant K_u in GdRh$_2$Si$_2$. (b) The negative of the basal anisotropy constant K_b. In both cases the results from in-plane and out-of-plane measurements are compared. See the main text for the definition of error bars.

additional basal anisotropy changes the *a*-axes ($\varphi_H = 0°, 90°$) into hard axes within this plane, whereas the [110]-axes are the easy axes. Thus, according to the definition in (4), K_b is negative in GdRh$_2$Si$_2$. As in the out-of-plane case, the anisotropy simulations fit the experimental data very well over a broad temperature range between 20 and 80 K. This is the case for $T = 5$ K, too, but the data are not shown here due to spectra of bad quality over a wider angular range. As before, the free fitting parameters are K_u and K_b only.

ESR data were additionally recorded at X-band microwave frequency. The resonance fields generally reflect the same behaviour as described above for the Q-band. The spectra can be well evaluated for temperatures $T > 60$ K. At lower temperatures, the signal weakens and gets disturbed by nonresonant low-field features in the spectra [2] due to a spin–flip transition aligning the magnetic sublattices from their ground state configuration to nearly perpendicular to the external field [1]. For 60 K and 80 K, we applied the parameters from the Q-band fits to the frequency of 9.4 GHz. Whereas the agreement to experimental data at 80 K is still acceptable, the simulation does not match the X-band data at 60 K. While the experimental data has, for rotations in the (*aa*)-plane, its minima at 1800 Oe, the simulation drops down to less than 600 Oe, where it becomes discontinuous. Section 3.3 takes up this issue in more detail.

3.2. Anisotropy constants of GdRh$_2$Si$_2$

Figure 6 summarises the anisotropy constants determined from the fits in section 3.1. Both kinds of field rotations provide an uniaxial constant K_u in the same order of magnitude, see figure 6(a). Rotations in the (*aa*)-plane seem more
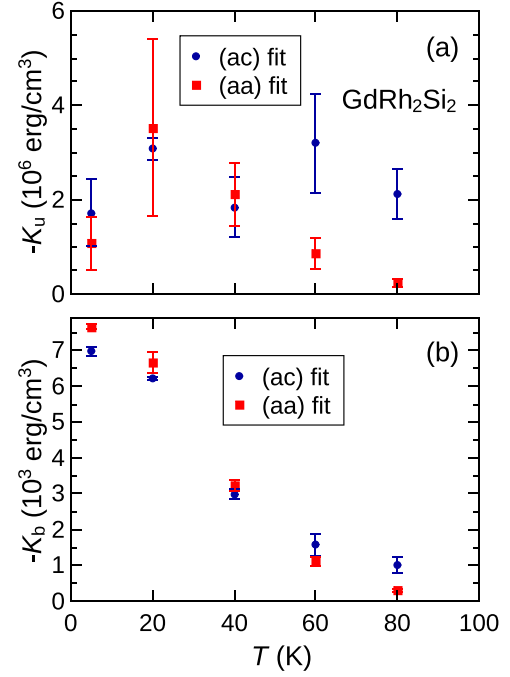
trustworthy, because they reproduce, except for the lowest temperature, a monotonous increase with decreasing temperature. Surprisingly, out-of-plane rotations, i.e. in the (*ac*)-plane, only suggest a rather constant K_u over the given temperature range and are, thus, considered less suitable for providing the uniaxial anisotropy constant. Indeed, the divergence of H_{res} towards the *c*-axis (see figure 4) is an intrinsic feature of easy-plane antiferromagnets and in first respect is not dependent on the magnitude of the negative K_u. Error bars in figure 6 are roughly estimated by variation of the respective anisotropy constant until the square deviations χ^2 of the fit get doubled. Thus, they indicate the borders where deviations in K would result in a similar error in the fit as compared to the remaining χ^2 at its minimum. Obviously, for K_u there is no satisfactory overlap between (*aa*)- and (*ac*)-measurements at 60 and 80 K. On the low-temperature side, the result for 5 K must even more be considered with caution. Experimentally it was difficult to obtain an ESR signal of reasonable strength at this temperature and it even was weakened further during both kinds of rotations, so that we could only access limited angular ranges. The reason therefore could not be clarified. Thus, we consider at least the value obtained for K_u at the lowest temperature unlikely and the seeming maximum at 20 K shall not be taken too serious. The neglection of the point at 5 K would allow an extrapolation of the more reliable (*aa*)-data to an order-of-magnitude estimation of the lowest-temperature value $K_u \approx -10 \times 10^6$ erg cm^{-3}, corresponding to an anisotropy field $H_u = |2K_u/M| = 50$ kOe. As shown by figure 6(a), a precise determination of K_u in this system is generally hard to be realized by antiferromagnetic resonance.

The reason why especially the (*ac*)-fits do not allow a satisfactory determination of K_u is that, contrary to the expectation, large variations of this constant only lead to a minor vertical shift of calculated resonance fields in figure 4. The main contribution to the shifts stems from the basal anisotropy constant K_b. The divergence of H_{res} towards $H \parallel c$ is characteristic for the considered type of antiferromagnet, irrespective of the detailed size of K_u, as long as $K_u < 0$. The fact of minor vertical shifts of calculated H_{res} upon large modification of K_u has been proven in the in-plane plots $H_{res}(\varphi_H)$ (figure 5), too. This is the reason, why also the (*aa*)-points in figure 6(a) partially have large errors.

Concerning the physical origin of anisotropy in GdRh$_2$Si$_2$, several mechanisms may be mentioned. Because of the spin-only magnetic moments of Gd^{3+} (ground state $^8S_{7/2}$), admixtures of excited atomic states are needed to account for a possible single-ion anisotropy, which however would only explain an anisotropy field less than 0.1 kOe and a similar estimate is obtained for the anisotropy due to dipolar interaction [19]. Instead exchange anisotropy as a microscopic origin of anisotropy has been discussed in the literature [19, 20].

Contrary to K_u, it must be noted that the basal anisotropy constant K_b (figure 6(b)) is generally more consistent between both kinds of measurements, out-of-plane and in-plane rotations. Error bars are small in the latter case. At 80 K the drop of K_b as determined by the (*aa*)-plane experiments seems more realistic and makes these measurements again preferable over the (*ac*)-plane experiments. And indeed it is considered natural that in-plane-rotations provide the basal anisotropy constant much more accurately. Nevertheless it is surprising that also the out-of-plane measurements give rather accurate results for the strength of the basal anisotropy. At low temperatures, K_b amounts to approximately -7000 erg cm^{-3}. The smallness of the basal anisotropy as compared to the dominant uniaxial term is worth to note and the reason why it is usually neglected [13].

Figure 7. Plots of calculated resonance frequencies ν_{res} versus external field H_0 for variation of different parameters. (a) The field direction is at the polar angle $\theta_H = 70°$ within the (*ac*)-plane and the basal anisotropy K_b is varied in steps of 1000 erg cm^{-3}. (b) θ_H is rotated within the (*ac*)-plane. (c) The azimuthal field angle φ_H is rotated within the (*aa*)-plane. In all three cases the uniaxial anisotropy $K_u = -1 \times 10^6$ erg cm^{-3}. In frames (b) and (c), $K_b = -5000$ erg cm^{-3}.

3.3. Calculated resonance frequencies

Pure simulations of resonance frequencies ν_{res} as a function of external field H_0 are plotted in figure 7. $M_0 = 400$ G and $\Lambda = 710$ are chosen as the low-temperature parameters for GdRh$_2$Si$_2$, $K_u = -1 \times 10^6$ erg cm^{-3} is taken in an order of magnitude realistic for GdRh$_2$Si$_2$ as well as $g = 2$. In figure 7(a) the field angles $\theta_H = 70°$ and $\varphi_H = 0°$ are selected and K_b, the anisotropy parameter which is mainly discussed in this work, is varied in steps of 1000 erg cm^{-3}. Starting with $K_b = 0$ a proportionality between H_0 and ν_{res} is observed with a slightly smaller slope than one would expect for a $g = 2$ paramagnet. That slope, however, is almost restored when setting $\theta_H = 90°$ (not shown in the figure), as can be seen from (7). When turning K_b positive, zero field resonances occur at finite frequencies, meaning that an excitation gap opens. This is because for positive K_b the easy axes of the basal anisotropy are along the *a*-axes, which also correspond to the approximate magnetisation directions in our calculation. Thus even at zero
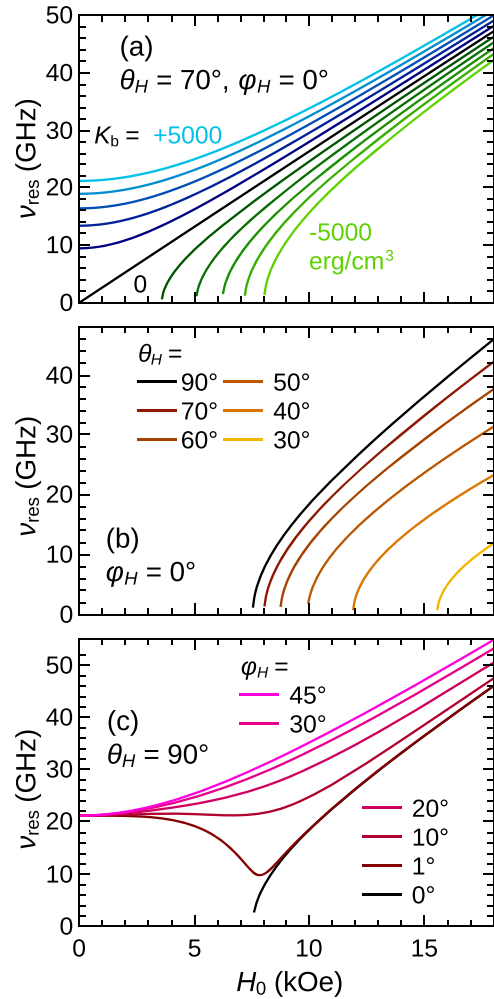
external field the sublattice magnetisations underlie the existing internal anisotropy field, yielding finite resonance frequencies at $H_0 = 0$. For $K_b < 0$ the curves in figure 7(a) bend in the opposite way and for low external fields the simulations fail. A spin reorientation transition takes place. At zero and low external fields the sublattice magnetisations are, in reality, along the diagonals between the *a*-axes. With increasing H_0, the $M^{(i)}$ turn continuously towards directions close to the *a*-axes and ν_{res} decreases, because internal and external fields counteract. When the magnetisation has become perpendicular to the external field, the resonance frequency can again increase with increasing field which is indeed seen in the simulations. As our model is based on the latter magnetisation configuration, the low field features are not captured in figure 7(a). Empirically, the excitation gaps for $K_b > 0$ observed in this figure match the well-known expression $\omega_{res} = \gamma\sqrt{2\Lambda M_0 H_{an}}$ [13], when defining the basal anisotropy field as $H_{an} = H_b := |8K_b/M_0|$.

The situation is similar in figure 7(b), where $K_b = -5000 \, \text{erg cm}^{-3}$ is fixed and the angle θ_H of the external field within the (ac)-plane is varied. The spin-reorientation transition is always observed, but its field value increases when tilting $\boldsymbol{H}_0$ away from the (aa)-plane. Moreover, the resonance frequency above this transition gets more and more suppressed. At $\theta_H = 0°$ one ends up with the aforementioned Goldstone mode $\nu_{res} = 0$. In figure 7(c) the same anisotropy constants are used, but the rotation now takes place within the (aa)-plane. For $\varphi_H = 0°$ the same situation as in figure 7(b) at $\theta_H = 90°$ is encountered. Increasing to $\varphi_H = 1°$ already lifts the minimal resonance frequency from 0 to 10 GHz, rendering the simulations possible even below the transition. The significant difference to out-of-plane simulations is here, that the azimuthal angles of the two sublattice magnetisations may differ from each other when employing in-plane simulations. As anticipated before, ν_{res}-curves in figure 7(c) approach a constant and finite value at zero field. The upwards trend is continued up to $\varphi_H = 45°$, where the situation now corresponds exactly to the case of $\varphi_H = 0°$ and $K_b = +5000 \, \text{erg cm}^{-3}$ in figure 7(a).

These field-frequency plots help to understand why the X-band data on $GdRh_2Si_2$ are not suitably described by our model. With too large anisotropy constants, the excitation gap is not overcome by the microwave energy. At higher temperatures, anisotropies are small and the excitation gap may still be overcome. But even then, the steep slopes in $\nu_{res}(H_0)$ when the external field is in the (ac)-plane or close to it as well as strong shifts of H_{res} at $\nu_{rf} = 9.4 \, \text{GHz}$ during field rotations destabilize the simulation.

4. Conclusions

From an application point of view, magnetic anisotropy gets its largest interest in magnetic thin films and bulk ferromagnets. Here, ESR is an important tool for its determination. The anisotropy in bulk antiferromagnets, however, is mostly measured by macroscopic magnetisation measurements, because typically the experimental access by ESR is difficult. With this work we could demonstrate that there are cases where the anisotropy in an antiferromagnet can nevertheless be well measured by conventional ESR. In $GdRh_2Si_2$, the angular dependences of resonance fields at Q-band frequency are excellently fitted by the model of two oscillating magnetic sublattices, using only two free parameters. The specific type of magnetic anisotropy includes an easy-plane uniaxial and an additional fourfold basal term. The uniaxial term is dominant with an anisotropy field at low temperatures of the order $H_u \approx 50 \, \text{kOe}$. With small uncertainty, we could quantify the basal anisotropy constant at low temperatures to $K_b \approx -7000 \, \text{erg cm}^{-3}$, giving by definition a basal anisotropy field of $H_b = |8K_b/M| \approx 140 \, \text{Oe}$. Supported by the agreement between experimental data and calculated resonance fields, it was safe to plot theoretical field-frequency diagrams which essentially support the idea of the basal anisotropy leading to an excitation gap and, depending on its sign or the field direction, possibly to a spin–flip transition. It turned out that magnetocrystalline anisotropy alone is

sufficient to describe ESR angular dependences, whereas we did not find clear indications for a possible anisotropy of the g-factor.

This experimental study and the excellent agreement between our theoretical modelling and the experimental results demonstrate that in magnetic systems with easy plane behaviour and weak in-plane anisotropy ESR experiments can provide a deep insight into anisotropic properties and interactions. On a more general level, we would like to emphasize that it is reasonable and worthwhile not only to consider the dominant uniaxial anisotropy, but also the weaker in-plane anisotropy. Our results provide a basis for the study and analysis of such systems. One of the most interesting candidates is the system $YbRh_2 2Si_2$. This sister compound to $GdRh_2Si_2$ is located extremely close to a quantum critical transition between an antiferromagnetic and a paramagnetic ground state. This results in very unusual properties, e.g. strong deviation from Fermi liquid behaviour, as well as a unique electronic–nuclear transition to a superconducting state. Therefore $YbRh_2Si_2$ has attracted very strong interest. However, because the size of the ordered moment is extremely small, of the order of $10^{-3} \, \mu_B$, and the ordering temperature is pretty small too, $T_N = 70 \, \text{mK}$, most of the characteristics of the AFM state are yet not clear. Fortunately $YbRh_2Si_2$ is an easy plane system with weak in-plane anisotropy as $GdRh_2Si_2$, and surprisingly a well-defined ESR can be observed despite the presence of a strong Kondo interaction [21]. Moreover, in preliminary experiments using a broad band technique, this ESR signal could be followed down to very low temperatures and low magnetic fields, well into the AFM state. Extending these experiments and analyzing the spectra using the models and knowledge developed in the present study on $GdRh_2Si_2$ shall likely allow to get much deeper insight into the magnetism and AFM state of $YbRh_2Si_2$, and thus provide important information to get an understanding of this paradigmatic quantum critical system.

Appendix A. Formulae for out-of-plane rotations

The formulae are in the primed framework of figure 2(a). Differing from the main text however, the primes of θ' and φ' are omitted here for better readability. The angles θ and φ in this appendix shall not be confused with θ and φ from the main text.

A.1. Equilibrium angles

$$\frac{\partial F}{\partial \theta} = 2H_0 M_0 \, \sin \, \varphi \, \sin(\theta - \theta_H) + 2K_u \, \sin \, 2\theta \, \sin^2 \, \varphi$$
$$+ \frac{2K_b}{D^3} \left\{ \sin^2 2\varphi \, \sin \, 2\theta [1 - \sin^2 \, \varphi(1 + \sin^2 \, \theta)] \right\},$$

$$\frac{\partial^2 F}{\partial \theta^2} = 2H_0 M_0 \sin \varphi \cos(\theta - \theta_H) + 4K_u \cos 2\theta \sin^2 \varphi$$
$$+ \frac{2K_b}{D^4} \sin^2 2\varphi \left\{ (2D \cos 2\theta - 3 \sin^2 2\theta \sin^2 \varphi) \right.$$
$$\times [1 - \sin^2 \varphi(1 + \sin^2 \theta)] - D \sin^2 2\theta \sin^2 \varphi \left. \right\},$$

$$\frac{\partial F}{\partial \varphi} = 2\Lambda M_0^2 \sin 2\varphi - 2H_0 M_0 \cos \varphi$$
$$\times \cos(\theta - \theta_H) - 2K_u \cos^2 \theta \sin 2\varphi$$
$$+ \frac{K_b}{D^3}(4D \sin^2 \theta \sin 4\varphi + \sin^2 2\theta \sin^3 2\varphi),$$

$$\frac{\partial^2 F}{\partial \varphi^2} = 4\Lambda M_0^2 \cos 2\varphi + 2H_0 M_0 \sin \varphi \cos (\theta - \theta_H)$$
$$- 4K_u \cos^2 \theta \cos 2\varphi + \frac{K_b}{D^4} \left\{ \left[16D \sin^2 \theta \cos 4\varphi \right. \right.$$
$$- \sin^2 2\theta \sin 2\varphi \sin 4\varphi + 6 \sin^2 2\theta \sin^2 2\varphi$$
$$\times \left. \cos 2\varphi \right] D + 3 \cos^2 \theta \sin 2\varphi$$
$$\times (4D \sin^2 \theta \sin 4\varphi + \sin^2 2\theta \sin^3 2\varphi) \left. \right\},$$

$$\frac{\partial^2 F}{\partial \theta \partial \varphi} = 2H_0 M_0 \cos \varphi \sin (\theta - \theta_H) + 2K_u \sin 2\theta \sin 2\varphi$$
$$+ \frac{K_b}{D^4} \left\{ [4 \sin 2\theta \sin 4\varphi(\sin^2 \theta \sin^2 \varphi + D) \right.$$
$$+ \sin 4\theta \sin^3 2\varphi] D - 3 \sin 2\theta \sin^2 \varphi$$
$$\times (4D \sin^2 \theta \sin 4\varphi + \sin^2 2\theta \sin^3 2\varphi) \left. \right\},$$

where $D = 1 - \cos^2 \theta \sin^2 \varphi$.

A.2. Elements of matrix A

Using $M_{x0} := M_{x0}^{(1)} = M_0 \cos \varphi$, $M_{y0} := M_{y0}^{(1)} = M_0 \sin \varphi$, $\eta := M_{y0} \sin\theta/M_{x0}$, $\omega_e := \gamma \Lambda M_0$, $\omega_u := 2K_u \gamma/M_0$ and $\kappa := 8K_b \gamma M_{y0} \sin \theta/(M_{x0})^2$, the matrix elements are

$$A_{11} = \gamma M_0 k_{zx} \sin \varphi + i\omega,$$

$$A_{12} = \gamma H_0 \sin(\theta - \theta_H) + \omega_u \sin 2\theta \sin \varphi$$
$$+ \gamma M_0 k_{zy} \sin \varphi + \kappa \cos \theta,$$

$$A_{13} = \omega_e \sin \varphi - \gamma H_0 \cos(\theta - \theta_H) + \omega_u \sin \varphi$$
$$\times (\sin^2 \theta - \cos^2 \theta) + \gamma M_0 k_{zz} \sin \varphi + \kappa \sin \theta,$$

$$A_{16} = -\omega_e \sin \varphi,$$

$$A_{21} = -\gamma H_0 \sin(\theta - \theta_H) - \frac{\omega_u}{2} \sin 2\theta \sin \varphi$$
$$- \gamma M_0 k_{zx} \cos \varphi - \kappa \cos \theta,$$

$$A_{22} = -\frac{\omega_u}{2} \sin 2\theta \cos \varphi - \gamma M_0 k_{zy} \cos \varphi + i\omega,$$

$$A_{23} = \omega_e \cos \varphi - \omega_u \sin^2 \theta \cos \varphi - \gamma M_0 k_{zz} \cos \varphi + \kappa\eta,$$

$$A_{26} = \omega_e \cos \varphi,$$

$$A_{31} = -\omega_e \sin \varphi + \gamma H_0 \cos(\theta - \theta_H) + \omega_u \cos^2 \theta \sin \varphi$$
$$+ \gamma M_0(k_{yx} \cos \varphi - k_{xx} \sin \varphi) - \kappa \sin \theta,$$

$$A_{32} = -\omega_e \cos \varphi + \omega_u \cos^2 \theta \cos \varphi$$
$$+ \gamma M_0(k_{yy} \cos \varphi - k_{xy} \sin \varphi) - \kappa\eta,$$

$$A_{33} = \frac{\omega_u}{2} \sin 2\theta \cos \varphi + \gamma M_0(k_{yz} \cos \varphi - k_{xz} \sin \varphi) + i\omega,$$

$$A_{34} = \omega_e \sin \varphi,$$

$$A_{35} = -\omega_e \cos \varphi,$$

$$A_{44} = -\gamma M_0 k_{zx} \sin \varphi + i\omega,$$

$$A_{55} = \frac{\omega_u}{2} \sin 2\theta \cos \varphi + \gamma M_0 k_{zy} \cos \varphi + i\omega,$$

$$A_{66} = -\frac{\omega_u}{2} \sin 2\theta \cos \varphi$$
$$- \gamma M_0(k_{yz} \cos \varphi - k_{xz} \sin \varphi) + i\omega,$$

and further $A_{43} = A_{16}$, $A_{45} = A_{12}$, $A_{46} = A_{13}$, $A_{53} = A_{35}$, $A_{54} = A_{21}$, $A_{56} = -A_{23}$, $A_{61} = A_{34}$, $A_{62} = A_{26}$, $A_{64} = A_{31}$, $A_{65} = -A_{32}$ as well as $A_{14} = A_{15} = A_{24} = A_{25} = A_{36} = A_{41} = A_{42} = A_{51} = A_{52} = A_{63} = 0$. The coefficients $k_{\alpha\beta}$, connecting dynamic magnetisation component β to dynamic basal field component α are

$$k_{xx} = -24K_b \eta^2/M_{x0}^2,$$
$$k_{xy} = 16K_b \eta \sin \theta/M_{x0}^2,$$
$$k_{xz} = -8K_b M_{y0} \sin 2\theta/M_{x0}^3,$$
$$k_{yy} = -8K_b \sin^2 \theta/M_{x0}^2,$$
$$k_{yz} = 4K_b \sin 2\theta/M_{x0}^2,$$
$$k_{zz} = -8K_b \cos^2 \theta/M_{x0}^2$$

and $k_{yx} = k_{xy}$, $k_{zx} = k_{xz}$, $k_{zy} = k_{yz}$.

Appendix B. Formulae for in-plane rotations

The formulae are in the primed framework of figure 2(b). Differing from the main text however, the primes of φ_1' and φ_2' are omitted here for better readability. The angles φ_1 and φ_2 in this appendix shall not be confused with φ_1 and φ_2 from the main text.

B.1. Equilibrium angles

$$\frac{\partial F}{\partial \varphi_1} = \Lambda M_0^2 \sin(\varphi_1 + \varphi_2)$$
$$- H_0 M_0 \cos \varphi_1 + 2K_b \sin[4(\varphi_1 - \varphi_H)],$$

$$\frac{\partial^2 F}{\partial \varphi_1^2} = \Lambda M_0^2 \cos(\varphi_1 + \varphi_2)$$
$$+ H_0 M_0 \sin \varphi_1 + 8K_b \cos[4(\varphi_1 - \varphi_H)],$$

$$\frac{\partial F}{\partial \varphi_2} = \Lambda M_0^2 \sin(\varphi_1 + \varphi_2)$$
$$- H_0 M_0 \cos \varphi_2 + 2K_b \sin[4(\varphi_2 + \varphi_H)],$$

$$\frac{\partial^2 F}{\partial \varphi_2^2} = \Lambda M_0^2 \ \cos(\varphi_1 + \varphi_2)$$

$$+ H_0 M_0 \ \sin \ \varphi_2 + 8K_{\mathrm{b}} \ \cos[4(\varphi_2 + \varphi_{\mathrm{H}})],$$

$$\frac{\partial^2 F}{\partial \varphi_1 \partial \varphi_2} = \Lambda M_0^2 \ \cos(\varphi_1 + \varphi_2).$$

B.2. Elements of matrix A

Using $M_{x\,0}^{(1)} = M_0 \ \cos \varphi_1$, $M_{y\,0}^{(1)} = M_0 \ \sin \varphi_1$, $M_{x\,0}^{(2)} = -M_0 \ \cos \varphi_2$, $M_{y\,0}^{(2)} = M_0 \ \sin \varphi_2$, $\omega_{\mathrm{e}} := \gamma \Lambda M_0$, $\omega_{\mathrm{u}} := 2K_{\mathrm{u}} \gamma / M_0$ and $\kappa := 2K_{\mathrm{b}} / M_0^4$, the matrix elements are

$$A_{13} = \omega_{\mathrm{e}} \ \sin \ \varphi_2 - \gamma H_0 + \omega_{\mathrm{u}} \ \sin \ \varphi_1 - \gamma H_{\mathrm{b}\,0\,y}^{(1)},$$

$$A_{16} = -\omega_{\mathrm{e}} \ \sin \ \varphi_1,$$

$$A_{23} = \omega_{\mathrm{e}} \ \cos \ \varphi_2 - \omega_{\mathrm{u}} \ \cos \ \varphi_1 + \gamma H_{\mathrm{b}\,0\,x}^{(1)},$$

$$A_{26} = \omega_{\mathrm{e}} \ \cos \ \varphi_1,$$

$$A_{31} = -\omega_{\mathrm{e}} \ \sin \ \varphi_2 + \gamma H_0 + \gamma H_{\mathrm{b}\,0\,y}^{(1)}$$
$$+ \gamma M_0 \left(k_{yx}^{(1)} \ \cos \ \varphi_1 - k_{xx}^{(1)} \ \sin \ \varphi_1 \right),$$

$$A_{32} = -\omega_{\mathrm{e}} \ \cos \ \varphi_2 - \gamma H_{\mathrm{b}\,0\,x}^{(1)}$$
$$+ \gamma M_0 \left(k_{yy}^{(1)} \ \cos \ \varphi_1 - k_{xy}^{(1)} \ \sin \ \varphi_1 \right),$$

$$A_{43} = -\omega_{\mathrm{e}} \ \sin \ \varphi_2,$$

$$A_{46} = \omega_{\mathrm{e}} \ \sin \ \varphi_1 - \gamma H_0 + \omega_{\mathrm{u}} \ \sin \ \varphi_2 - \gamma H_{\mathrm{b}\,0\,y}^{(2)},$$

$$A_{53} = -\omega_{\mathrm{e}} \ \cos \ \varphi_2,$$

$$A_{56} = -\omega_{\mathrm{e}} \ \cos \ \varphi_1 + \omega_{\mathrm{u}} \ \cos \ \varphi_2 + \gamma H_{\mathrm{b}\,0\,x}^{(2)},$$

$$A_{64} = -\omega_{\mathrm{e}} \ \sin \ \varphi_1 + \gamma H_0 + \gamma H_{\mathrm{b}\,0\,y}^{(2)}$$
$$- \gamma M_0 \left(k_{yx}^{(2)} \ \cos \ \varphi_2 + k_{xx}^{(2)} \ \sin \ \varphi_2 \right),$$

$$A_{65} = \omega_{\mathrm{e}} \ \cos \ \varphi_1 - \gamma H_{\mathrm{b}\,0\,x}^{(2)}$$
$$- \gamma M_0 \left(k_{yy}^{(2)} \ \cos \ \varphi_2 + k_{xy}^{(2)} \ \sin \ \varphi_2 \right),$$

and further $A_{11} = A_{22} = A_{33} = A_{44} = A_{55} = A_{66} = \mathrm{i}\omega$, $A_{12} = A_{14} = A_{15} = A_{21} = A_{24} = A_{25} = A_{36} = A_{41} = A_{42} = A_{45} = A_{51} = A_{52} = A_{54} = A_{63} = 0$ as well as $A_{34} = -A_{16}$, $A_{35} = -A_{26}$, $A_{61} = -A_{43}$, $A_{62} = -A_{53}$. Static basal field components and dynamic basal coefficients for the two sublattices $i = 1, 2$ are

$$H_{\mathrm{b}\,0\,x}^{(i)} = 2\kappa \left[\frac{3}{2} \left(M_{x\,0}^{(i)} \right)^2 M_{y\,0}^{(i)} \ \sin \ 4\varphi_{\mathrm{H}} - \left(M_{x\,0}^{(i)} \right)^3 \sin^2 2\varphi_{\mathrm{H}} \right],$$

$$H_{\mathrm{b}\,0\,y}^{(i)} = \kappa \left(M_{x\,0}^{(i)} \right)^2 \left[M_{x\,0}^{(i)} \ \sin \ 4\varphi_{\mathrm{H}} \right.$$
$$\left. + 2M_{y\,0}^{(i)} \left(\sin^2 2\varphi_{\mathrm{H}} - 2 \cos^2 2\varphi_{\mathrm{H}} \right) \right],$$

$$k_{xx}^{(i)} = 2\kappa \left[M_{x\,0}^{(i)} M_{y\,0}^{(i)} \ \sin \ 4\varphi_{\mathrm{H}} - \left(M_{x\,0}^{(i)} \right)^2 \sin^2 2\varphi_{\mathrm{H}} \right.$$
$$\left. - 2 \left(M_{y\,0}^{(i)} \ \cos \ 2\varphi_{\mathrm{H}} - M_{x\,0}^{(i)} \ \sin \ 2\varphi_{\mathrm{H}} \right)^2 \right],$$

$$k_{xy}^{(i)} = \kappa \left[4 \left(M_{x\,0}^{(i)} \ \cos \ 2\varphi_{\mathrm{H}} + M_{y\,0}^{(i)} \ \sin \ 2\varphi_{\mathrm{H}} \right) \right.$$
$$\times \left(M_{x\,0}^{(i)} \ \sin \ 2\varphi_{\mathrm{H}} - M_{y\,0}^{(i)} \ \cos \ 2\varphi_{\mathrm{H}} \right)$$
$$\left. - 4M_{x\,0}^{(i)} M_{y\,0}^{(i)} \ \cos^2 2\varphi_{\mathrm{H}} + \left(M_{x\,0}^{(i)} \right)^2 \ \sin \ 4\varphi_{\mathrm{H}} \right],$$

$$k_{yx}^{(i)} = \kappa M_{x\,0}^{(i)} \left[3M_{x\,0}^{(i)} \ \sin \ 4\varphi_{\mathrm{H}} \right.$$
$$\left. - 4M_{y\,0}^{(i)} \left(2 \cos^2 2\varphi_{\mathrm{H}} - \sin^2 2\varphi_{\mathrm{H}} \right) \right],$$

$$k_{yy}^{(i)} = 2\kappa M_{x\,0}^{(i)} \left[M_{x\,0}^{(i)} \left(\sin^2 2\varphi_{\mathrm{H}} - 2 \cos^2 2\varphi_{\mathrm{H}} \right) \right.$$
$$\left. - 3M_{y\,0}^{(i)} \ \sin \ 4\varphi_{\mathrm{H}} \right].$$

ORCID iDs

D Ehlers https://orcid.org/0000-0002-4628-6126
K Kliemt https://orcid.org/0000-0001-7415-4158

References

[1] Kliemt K, Hofmann-Kliemt M, Kummer K, Yakhou-Harris F, Krellner C and Geibel C 2017 *Phys. Rev.* B **95** 134403
[2] Sichelschmidt J, Kliemt K, Hofmann-Kliemt M and Krellner C 2018 *Phys. Rev.* B **97** 214424
[3] Gegenwart P, Si Q and Steglich F 2008 *Nat. Phys.* **4** 186
[4] Si Q and Steglich F 2010 *Science* **329** 1161
[5] von Löhneysen H, Rosch A, Vojta M and Wölfle P 2007 *Rev. Mod. Phys.* **79** 1015
[6] Trovarelli O, Geibel C, Mederle S, Langhammer C, Grosche F M, Gegenwart P, Lang M, Sparn G and Steglich F 2000 *Phys. Rev. Lett.* **85** 626
[7] Schuberth E *et al* 2016 *Science* **351** 485
[8] Gruner T, Sichelschmidt J, Klingner C, Krellner C, Geibel C and Steglich F 2012 *Phys. Rev.* B **85** 035119
[9] Ishida K *et al* 2003 *Phys. Rev.* B **68** 184401
[10] Hamann S *et al* 2019 *Phys. Rev. Lett.* **122** 077202
[11] Momma K and Izumi F 2011 *J. Appl. Crystallogr.* **44** 1272
[12] Kliemt K and Krellner C 2015 *J. Cryst. Growth* **419** 37–41
[13] Gurevich A G and Melkov G A 1996 *Magnetization Oscillations and Waves* (Boca Raton, FL: CRC Press)
[14] Sichelschmidt J, Kliemt K, Krellner C and Geibel C 2017 *J. Phys.: Conf. Ser.* **807** 012007
[15] Ehlers D, Tsurkan V, Krug von Nidda H A and Loidl A 2012 *Phys. Rev.* B **86** 174423
[16] Tsurkan V, Lohmann M, Krug von Nidda H A, Loidl A, Horn S and Tidecks R 2001 *Phys. Rev.* B **63** 125209
[17] Tsurkan V, Mücksch M, Krug von Nidda H-A, Hemberger J, Samusi D, Loidl A, Horn S and Tidecks R 2002 *Solid State Commun.* **123** 327
[18] Morrish A H 1965 *The Physical Principles of Magnetism* (New York: Wiley)
[19] Czjzek G, Oestreich V, Schmidt H, Łąka K and Tomala K 1989 *J. Magn. Magn. Mater.* **79** 42
[20] Wendler R, Pureur P, Fert A and Baberschke K 1984 *J. Magn. Magn. Mater.* **45** 185
[21] Sichelschmidt J, Ivanshin V A, Ferstl J, Geibel C and Steglich F 2003 *Phys. Rev. Lett.* **91** 156401